Surface reactivity of Li2MnO3: first-principles and experimental study

Ambroise Quesne-Turin, Delphine Flahaut, Laurence Croguennec, Germain Vallverdu, Joachim Allouche, Youn Charles-Blin, Jean-Noel Chotard, Michel Ménétrier, Isabelle Baraille

The surface reactivity of Li_2MnO_3: First principles and experimental study

Ambroise Quesne-Turin[1,2,4], Delphine Flahaut[1,4,], Laurence Croguennec[2,4], Germain Vallverdu[1,4], Joachim Allouche[1], Youn Charles-Blin[1,4], Jean-Noël Chotard[3,4], Michel Ménétrier[2,4] and Isabelle Baraille[1,4]*

[1] CNRS/ Univ. Pau & Pays Adour, Institut des Sciences Analytiques et de Physico-chimie pour l'Environnement et les Matériaux, UMR5254, F-64000 Pau, France

[2] CNRS, Univ. Bordeaux, Bordeaux INP, ICMCB UPR 9048, F-33600 Pessac, France

[3] Laboratoire de Réactivité et Chimie des Solides, CNRS-UMR#7314, Université de Picardie Jules Verne, F-80039 Amiens Cedex 1, France.

[4] RS2E, Réseau Français sur le Stockage Electrochimique de l'Energie, FR CNRS 3459, F-80039 Amiens Cedex 1, France

Corresponding Author

*Delphine Flahaut

delphine.flahaut@univ-pau.fr

KEYWORDS: Surface reactivity, XPS, single crystal, AES, first-principle calculations

ABSTRACT

The present paper deals with the surface reactivity of (001) oriented Li_2MnO_3 crystals investigated from a multi-techniques approach combining, material synthesis, X-ray photoemission spectroscopy (XPS), Scanning Electron Microscopy (SEM), Auger Electron Spectroscopy (AES) and first-principle calculations. Li_2MnO_3 is considered as a model compound suitable to go further in the understanding of the role of tetravalent manganese atoms in the surface reactivity of layered lithium oxides. The knowledge of the surface properties of such materials is essential in order to understand the mechanisms involved in parasitic phenomena responsible for early aging or poor storage performances of lithium-ion batteries. The surface reactivity was probed through the adsorption of SO_2 gas molecules on large Li_2MnO_3 crystals in order to be able to focus the XPS beam on the top of the (001) surface. A chemical mapping and XPS characterization of the material before and after the SO_2 adsorption show in particular that the adsorption is homogeneous at the micro and nanoscale and involves Mn reduction, while first-principle calculations on a slab model of the surface allow us to conclude that the most energetically favorable species formed is a sulfate with charge transfer implying reduction of Mn.

1. INTRODUCTION

The layered oxide $LiCoO_2$ is still currently the material mostly used at the positive electrode in commercial Lithium-ion batteries.[1] Other compositions of layered oxides have however been studied and commercialized, such as $LiNi_{0.80}Co_{0.15}Al_{0.05}O_2$ (belonging to the NCA family) and $LiNi_{1/3}Mn_{1/3}Co_{1/3}O_2$ (the so-called 1/3-1/3-1/3 NMC). The latter is the best alternative to $LiCoO_2$, with a larger capacity (140 $mAh.g^{-1}$ for $LiCoO_2$ with the upper voltage limited to 4.2 V

vs Li^+/Li and 170 $mAh.g^{-1}$ for this NMC with the upper voltage limited to 4.5 V vs Li^+/Li) and a better cyclability.[2] Its main advantages are in fact its lower cost and toxicity, due to the lower content in Co, as well as its higher thermal stability in the delithiated state, i.e. in the charged state of the battery. The large amount of Mn^{4+} (i.e. 1/3 of the transition metal ions), which remains stable when increasing temperature, stabilizes the layered structure and postpones to higher temperatures all the chemical processes involved during the thermal degradation of $Li_xNi_{1/3}Mn_{1/3}Co_{1/3}O_2$, i.e. the cationic migrations, the oxygen loss and the resulting reduction of the transition metal ions.

Layered oxides are known to undergo a partial dissolution of the transition metals in the electrolyte. The rate of these parasitic phenomena strongly depends on the cycling conditions (temperature, potential window …) and, especially, on both aging and storage conditions. The study of the surface reactivity is thus essential in order to understand the mechanisms involved in these dissolution processes and to propose solutions to this problem. For example, the coating of the surface of the layered oxide (by Al_2O_3, ZrO_2, …) has been proposed a few years ago and seems to be quite efficient to modify the surface reactivity and improve the range of cyclability[3–10]. Among the limited number of surface reactivity studies[11], Andreu *et al*.[12] proposed an original method based on the adsorption of gaseous probes at the extreme surface of the electrode material monitored by X-ray photoemission spectroscopy (XPS). They performed an in-depth analysis of the acidic and redox reactions occurring at the extreme surface of $LiMO_2$ layered oxides (M = Co, Mn, $Ni_{1/3}Mn_{1/3}Co_{1/3}$) and have shown an evolution of the surface reactivity depending on the transition metal composition and on the presence (or not) of a coating of Al_2O_3. For instance, the surface reactivity decreases with the formation of the coating and the change in the nature and amount of the adsorbed species. In order to deepen fundamental understanding of

the surface reactivity of $LiMO_2$, we have extended these studies to the model compound Li_2MnO_3 with the aim to fully explain the surface reactivity of the 1/3-1/3-1/3 NMC. A few results have been already obtained for the layered oxide $LiMnO_2$, rich in Mn^{3+}, where the surface reactivity is described in term of formal oxidation degrees and highlight the role of sub-surface transition metal ions in the surface reactivity of lamellar compounds.[13] Nevertheless, as manganese is at the tetravalent state in the ($LiNi^{II}_{1/3}Mn^{IV}_{1/3}Co^{III}_{1/3}O_2$) NMC, Li_2MnO_3 that can also be described as $Li[Li_{1/3}Mn^{IV}_{2/3}]O_2$ appears as the material of choice as a model for the NMC. In addition, Li_2MnO_3 is a Li and Mn^{4+} rich layered oxide material with lithium in excess in the transition metal layers.[14] It is particularly suitable for understanding the surface reactivity of the Li-rich and Mn-rich layered oxides (the so-called high energy NMC's) expected to be the next generation of positive electrode materials for Lithium-ion batteries as they deliver high reversible discharge capacity involving both cationic and anionic redox[4, 5, 15]

In this paper, a complete study of the surface reactivity of an Li_2MnO_3 crystal (001) surface was performed, both experimentally and theoretically using a multi-techniques methodology. On the basis of previous work,[12,16] the surface reactivity was investigated by adsorption of the SO_2 gas probe to measure the acidic and redox properties of the surface. The set of techniques used in this work allow us to obtained surface information, either at the nanoscale, or for the entirety of the sample depending on the size of the irradiation beam, the calculations providing nanoscale information by essence. The adsorbed species were identified from X-ray photoelectron spectroscopy (XPS) and the underlying electronic processes were analyzed from first-principle calculations. The morphology of the surface and the chemical mapping were obtained from Scanning Electron Microscopy (SEM) and Auger Electron Spectroscopy (AES).

2. EXPERIMENTAL SECTION

2.1. Material preparation

The synthesis route was adapted from the one reported by Tang *et al.*,[14] in order to promote the growth of crystals of Li_2MnO_3 large enough to be analyzed as a single crystal with the XPS spot whose size is 700 x 400 μm^2. We dissolved 5 g of $KMnO_4$ (Aldrich, purity of 99%) in 400 mL of water and 5 mL of ethanol. This solution was heated during 24 h at 100 °C in an autoclave. The manganese oxyhydroxyde phase γ-$Mn^{III}O(OH)$ thus obtained was washed with water first and ethanol then, ground with LiCl (Alfa Aesar, purity of 99% min.) so that the ratio Li/Mn is 10 (i.e. with a large excess of lithium). Finally, this mixture was heated at 4 °C.min^{-1} up to 650 °C and maintained at this temperature during 4 days, before being cooled down slowly (0.01 °C.min^{-1}) to ambient temperature.

2.2. Surface analyses

2.2.1. X-Ray Photoelectron Spectroscopy (XPS)

XPS analyses were performed on a Kratos Axis Ultra spectrometer with a focused monochromatized Al Kα radiation (1486.6 eV) in order to characterize the atomic composition and chemical environment of the elements at the surface of the samples (in a depth smaller than 10 nm). The analysis chamber was in a 5x10^{-9} mbar vacuum. The applied current was 12 mA and the voltage 12 kV. The spectrometer pass energy was set to 20 eV to record the core peaks. The size of the excitation beam was 700x400 μm^2. Surface charging was minimized using a neutralizer gun which sprays low energy electrons over the sample surface. The samples were prepared in a glove box under Ar and transferred to the XPS analyzer under a controlled

atmosphere to prevent any surface contamination with ambient atmosphere. The samples were fixed on the sample holder with a Cu double tape. All the binding energy (B.E.) scale was calibrated from the adventitious carbon C 1s peak set at 285.0 eV. We performed at last three analyses for each sample. The quantification of atoms for surface composition was based on Scofield's relative sensitivity factors[17].

2.2.2. Auger Electron-Spectroscopy (AES)

Surface morphology and chemical composition analyses were carried out on a JEOL JAMP 9500F Auger spectrometer (JEOL Ltd, Tokyo, Japan) working under ultra-high vacuum conditions (< 2 x 10^{-9} mbar), this spectrometer being a Schottky Field Emission Auger Electron Spectrometer (FE-AES) dedicated to very high spatial resolution and high brightness analyses. The excitation beam is ~6-10 nm in diameter. The hemi-spherical electron analyzer is coupled with a multichannel detector. The crystal is fixed on the sample holder with Ag paste.

2.2.3. Gas probe adsorption

The SO_2 adsorption was performed on a Micromeritics Autochem 2920 Analyzer. The Li_2MnO_3 crystal was introduced in a reactor and the surface was cleaned of physisorbed species with an argon flux at 632.15 K for 4 h (activation step). After the surface cleaning, the temperature was reduced to 353.15 K under a helium flux for 1h. The SO_2 adsorption step was then performed at 353.15 K for 15 min under a flux composed of 0.02% SO_2 in helium (50 $mL.min^{-1}$). The last step was a surface cleaning of physisorbed species, under a helium flux at 353.15 K for 1h. The gas probe adsorption was performed three times for most of the samples to ensure the reproducibility of the experiments. After adsorption, the samples were transferred into a glove box before being analyzed, always without being exposed to ambient atmosphere.

The SO_2 gaseous probe allows the investigation of acidic-basic and redox properties. A reaction between SO_2 and one oxygen atom of the extreme surface leads to the formation of a sulfite species (SO_3^{2-}), characterized by an S $2p_{3/2}$ core peak binding energy at 167.5 eV[12]. A reaction between SO_2 and two extreme surface oxygen atoms leads to the formation of sulfate species (SO_4^{2-}) characterized by an S $2p_{3/2}$ core peak binding energy at 169 eV[12]. The type and the amount of adsorbed species are characterized by X-Ray photoelectron spectroscopy analysis.

2.3. Computational details

The Electronic structure analyses were undertaken from density functional theory (DFT) calculations in 2D or 3D periodic boundary conditions for surface and bulk systems respectively. The surfaces were represented by the commonly used slab model (see Figure S1 in the supplementary information for more details) which consists in the stacking of several atomic layers parallel to a given lattice plane characterized by its (hkl) indices. A vacuum volume of at least 12 Å was left free between the slabs in order to quench spurious interactions between periodic images. In this context, the surface formation energy E_{surf}^{hkl} reads

$$E_{surf}^{hkl} = \frac{1}{2S}\left(E_{slab}^{hkl} - nE_{bulk}\right) \quad (1)$$

where E_{slab}^{hkl} and E_{bulk} are the energy of the bare slab parallel to the (hkl) planes and that of the bulk system respectively; n is the number of bulk unit formula in the slab and S is the surface area of the slab. The number of atomic layers included in the slab model was chosen in order to get a converged value for the surface formation energies. Moreover, we also checked that the electronic properties of atoms embedded at the center of the slab were closed to those of bulk atoms.

The adsorption of SO_2 molecules at the surface of Li_2MnO_3 was done by considering only the anionic sites. Top (1-fold) and bridge (2-fold) sites were investigated and led to the formation of sulfite (SO_3^{2-}) and sulfate (SO_4^{2-}) species respectively. The adsorption energy on an (hkl) surface for a given site, E_{ads}, was computed from

$$E_{ads} = E_{slab+SO_2}^{hkl} - E_{slab}^{hkl} - E_{SO_2} \quad (2)$$

where $E_{slab+SO_2}^{hkl}$ is the energy of the slab with one SO_2 molecule adsorbed and E_{SO_2} is the energy of an isolated SO_2 molecule computed in a cubic box of 10 Å length. The approach is detailed more in depth in our previous works.[13, 16]

All calculations were performed with the Vienna Ab initio Simulation Package [18, 19] (VASP) with the GGA functional PW91 of Perdew and Wang [20, 21] The wave-functions were described in the Projected Augmented Wave [22] (PAW) formalism with a plane waves basis set truncated at a cut-off energy of 700 eV. Valence electrons described explicitly in the calculations were $1s^2 2s^1$ for lithium atoms, $4s^2 3d^5$ for manganese atoms and $2s^2 2p^4$ for oxygen atoms. The Brillouin zone integration was done on a k-points grid uniformly distributed around the origin (Γ point) using a mesh of $4 \times 3 \times 3$ for bulk calculations and $4 \times 4 \times 1$ for surface calculations of 1×1 slab models. Charges calculations were performed by using Bader's topological analysis.[23]For bulk calculations, all degrees of freedom were fully relaxed whereas the cell shape and volume were kept fixed and only atomic positions of the first atomic layers were relaxed in the case of surface calculations.

Manganese atoms of Li_2MnO_3 present strongly localized 3d electrons for which DFT approach failed to describe accurately the electronic structure. Therefore, DFT+U calculations were undertaken using the rotationally invariant approximation of Dudarev *et al*.[24] In that case, the relevant Hubbard parameter is the spherically averaged, single effective parameter $U_{eff} = U - J$,

named hereafter U. The U parameter used in our calculation was 5.0 eV, which was determined for Mn^{4+} species[25] and commonly used for lithium layered oxides with manganese atoms.[26, 27] All calculations were done considering spin polarization with a ferromagnetic ordering. The magnetic moments of each atom were computed from the difference between the spin up and spin down electronic densities. Although one must keep in mind that electrons are delocalized, magnetic moments were used as a descriptor in order to suggest simple schemes in terms of formal oxidation degrees. The magnetic moments of manganese atoms in MnO, Mn_2O_3 and MnO_2 compounds were computed using the above conditions and were found to be 4.7 μ_B, 4,1 μ_B and 3.3 μ_B for Mn^{+II}, Mn^{+III} and Mn^{+IV} respectively. These values are therefore used as a reference in the analysis of the manganese redox in the Li_2MnO_3 system. More details are provided in supporting information.

3. RESULTS AND DISCUSSION

3.1. The bare material Li_2MnO_3

3.1.1. Structural characterization

The X-ray diffraction (XRD) pattern given in Figure 1 was collected on a PANalytical Empyrean diffractometer, in transmission mode, with the copper radiation ($K_{\alpha1}$ = 1.5405980 Å and $K_{\alpha2}$ = 1.5444260 Å) and in the [8-80°] angular range with a total acquisition time of 6h30. Pseudo-hexagonal platelet crystals of Li_2MnO_3 were crushed in order to be introduced in a capillary. All the diffraction lines can be indexed in a unit cell described in the monoclinic space group C2/m as reported for the first time by Strobel *et al.*[28]. The lattice parameters determined by the Le Bail method are $a_{C2/m}$ = 4.931(3) Å, $b_{C2/m}$ = 8.526(6) Å, $c_{C2/m}$ = 5.020(4) Å and $\beta_{C2/m}$ = 109.09(7)°.

Note that the peaks (020), (111), (-111), (021) and (111), theoretically expected in the 20°-34° (2θ) angular range, are merged in a single diffused asymmetric peak. As reported by Boulineau *et al.*,[29,30] this broadening reveals the presence of faults in the stacking of the ordered $[Li_{1/3}Mn_{2/3}]O_2$ slabs along the $[001]_{C2/m}$ direction, at least 50% as estimated from the comparison with Figures 4 and 5 from reference 29. Furthermore, as expected from the shape of the pristine (not crushed) crystals, the XRD pattern of the crushed crystals reveals a preferential orientation along the $[001]_{C2/m}$ crystallographic direction, suggesting that the (001) crystallographic planes are parallel to the larger faces of the platelets. This face indexation was furthermore confirmed by an X-ray diffraction study performed on a series of crystals similar to that given in inset in Figure 1. For the face indexing, the pseudo-hexagonal platelet Li_2MnO_3 single crystals were mounted on a Bruker D8 Venture diffractometer equipped with a Photon 100 CMOS detector and a *Mo-Kα* radiation source (λ = 0.71073 Å). Based on the unit cell determination, found to be in good agreement with that determined from powder X-ray diffraction results, and the corresponding orientation matrix of the crystal, face indexing was done using the APEX 3 software from Bruker. It reveals that the large flat face of the crystal corresponds to the (001) plane. The size of the representative crystal given in inset in Figure 1 is 0.040×0.582×0.792 mm^3, and thus large enough to be studied as a single crystal by XPS.

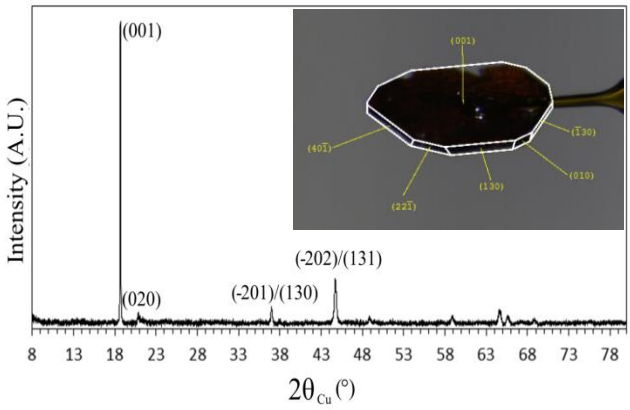

Figure 1. XRD pattern of the Li_2MnO_3 sample collected in transmission mode in a capillary. The diffraction lines are indexed using the monoclinic C2/m space group. In inset is given the image of one representative Li_2MnO_3 crystal with all its faces indexed (crystal size: 0.040×0.582×0.792 mm).

3.1.2. Surface characterization of the crystals

The surface morphology of the Li_2MnO_3 crystals was analyzed with a secondary electron scanning microscope. The crystal surface is flat with some terraces and islands, as shown by the scanning electron microscopy image given in Figure S2a in supporting information. Auger Electron Spectroscopy analyses were performed on the crystal surface in order to evaluate the homogeneity in terms of chemical composition. The excitation beam was focused on three target dots on the crystal surface as highlighted by red crosses in Figure S2a. The corresponding Auger spectra given in Figure S2b exhibit O KLL (460-520 eV) and Mn LMM (525-645 eV) transitions for all target dots. The C KLL (220-280 eV) transition is related to hydrocarbonated contaminations usually present on the surface of materials. The Li KLL transition located around 36 eV could not be extracted from the signal of the secondary electron background in this energy region. Finally, the Auger mapping in Figure S3 confirms the homogeneous chemical

composition of the material with the even location of the Mn, C and O signals on the whole Li_2MnO_2 surface.

All the XPS core peaks characteristic of the Li_2MnO_3 material (Mn 2p, Mn 3s, O 1s, Li 1s) and of the adventitious hydrocarbon were recorded. The corresponding binding energies and atomic percentages are reported in Table 1.

	B.E. (eV)	**At. %**
Mn $2p_{3/2}$	642.3	14.9
O 1s	529.7	28.9
	531.4	13.0
		41.9
C 1s	285.0	16.0
	286.5	3.8
	287.9	0.6
	288.9	2.2
		22.6
Li 1s	54.4	20.2
	55.3	0.4
		20.6

Table 1. Binding energy (eV) and Atomic percentages (%) of the Mn, O, C and Li elements obtained from XPS spectra of the Li_2MnO_3 crystal.

The Mn 2p spectrum of the bare crystal (before adsorption) is presented in Figure 2. Due to the spin-orbit coupling, the Mn 2p spectrum consists of two main components Mn $2p_{1/2}$ and Mn $2p_{3/2}$ located at 654.3 eV and 642.3 eV respectively with an area ratio of 1/2. The "shake-up" satellite is observed for the Mn $2p_{1/2}$ component at a binding energy higher by 11 eV, whereas that

associated to the Mn $2p_{3/2}$ is merged with the main Mn $2p_{1/2}$ component. Those binding energies are typical of a manganese atom in a tetravalent oxidation state (Figure S4).[31, 32] Moreover, the oxidation state of the manganese cation can be further confirmed by the B.E. splitting value of the Mn 3s core peak (Figure S5). This splitting is 4.5 eV, which is also characteristic of Mn^{4+}.[33] By this way, we can confirm the unique oxidation state (Mn^{4+}) of the manganese ions at the (001) crystal surface. The other core peaks, O 1s and Li 1s, are presented and discussed in the Figure S6. They are in accordance with expectations.

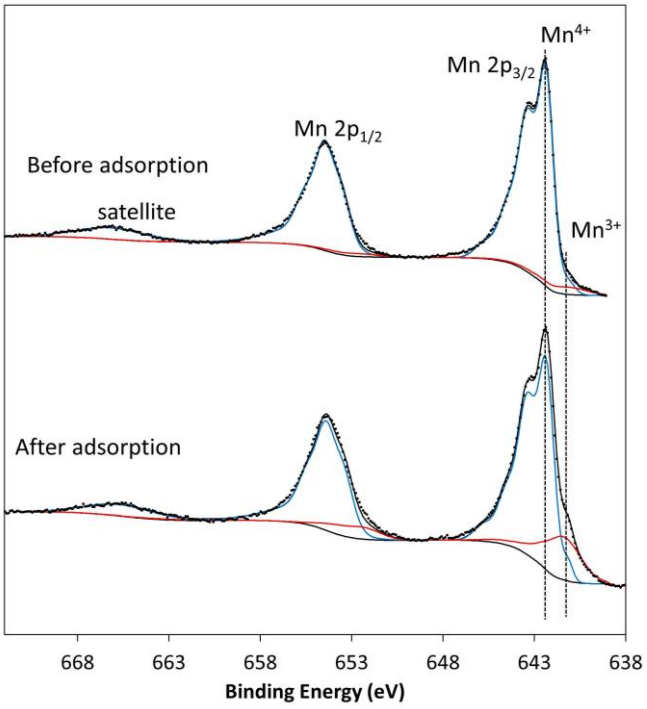

Figure 2. Mn 2p core peaks for the Li_2MnO_3 crystal, before surface cleaning (top spectrum) and after SO_2 adsorption (bottom spectrum). Black dots are experimental data, the red curve is associated to Mn^{3+} signal and the blue curve to Mn^{4+}.

3.1.3. Calculations of the electronic structures

Bulk

The structural optimization of an ideal Li_2MnO_3 bulk was performed in the monoclinic space group C2/m. The computed lattice parameters (a = 4.98 Å, b = 8.63 Å, c = 5.08 Å and β = 109.36°) are in good agreement with experimental values (the relative difference is less than 1.5%). Figure 3 gives the computed total density of states (DOS) calculated as the sum of projected DOS on O 2s, O 2p and Mn 3d atomic orbitals modulated by the photoionization cross sections from Scofield work[17], compared with the XPS valence spectrum of Li_2MnO_3 The calculated spectrum shows two main regions, one around -18 to -16 eV assigned to the O 2s levels and the second between -6 eV and the Fermi level corresponding to the contribution of the O 2p and Mn 3d levels. The qualitative agreement between the experimental and the theoretical spectra, considering in particular the width of the second band confirms the choice of the U value for the DFT+U calculations. The computed magnetic moment of Mn atoms is 3.2 μ_B which agrees well with formal Mn^{4+} species in Li_2MnO_3 (see Supporting Information, Table S1).

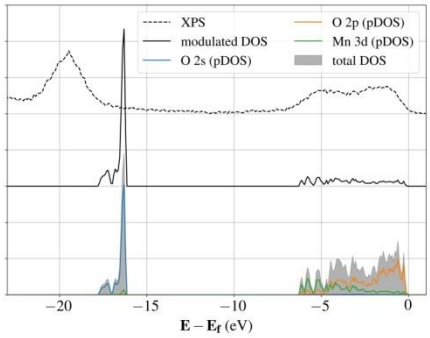

Figure 3. XPS valence band (dashed line), density of states (DOS) modulated by photoionization cross-sections (solid line) and projected density of states (pDOS) on O 2s, O 2p and Mn 3d atomic orbitals.

Bare slab

An exhaustive theoretical investigation of Li_2MnO_3 surfaces was carried out by Shin and Persson [34] who computed the surface formation energies of all low index surfaces with several terminations when relevant. Among them, we focused on the (001) surface with two different terminations as described in Figure 4. The (001) surface, classified as Tasker type III, is perpendicular to the stacking direction and is commonly expected for such a layered material. Four different types of (001) crystallographic planes exist, containing alternately oxygen anions only, Li^+ and Mn^{4+} cations ordered in octahedral sites in such a way that Li/Mn is 1/2, oxygen anions only, and finally Li^+ cations only.[30] We investigated two different terminations (001)-O and (001)-Li. First, in the (001)-O model (see Figure 4b), the last atomic layer contains only oxygen atoms. A symmetric slab model was built in order to remove the surface dipole moment. Second, the (001)-Li model (see Figure 4c) corresponds to a redistribution of half of the lithium atoms of the last atomic layer on both sides of the model in order to remove the surface dipole. On the last atomic layer, one third of the Li atoms are in octahedral sites while the other two thirds are in two types of tetrahedral sites, one of which occupied by manganese atoms in the bulk structure [34]. It was the most stable (001)-Li surface model calculated among all the systems considered by Shin and Persson[34] and we obtained a surface formation energy of 0.85 $J.m^{-2}$ (compare to 0.98 $J.m^{-2}$ obtained by Shin and Persson[34]).

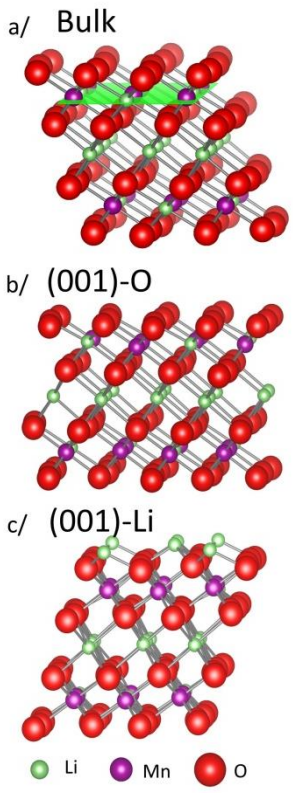

Figure 4. (a): Bulk structure of Li_2MnO_3, with an example of the (001) lattice plane (green). (b) and (c) give the side views of the first atomic layers of the O-terminated (001), called (001)-O, and the reconstructed Li-terminated (001), called (001)-Li, surfaces. The calculations on the adsorbed surfaces were done on the top layer of models b and c.

In the case of both (001) surface models, the octahedral environment of Mn atoms was conserved after the structural relaxation. On the top surface layers of the (001)-O surface, Mn-O bond lengths lie between 1.87 and 1.96 Å, in comparison to 1.93 Å in the bulk structure, and are associated to a tiny packing of these two first atomic layers. They remain unchanged in deeper atomic layers as well as in the (001)-Li surface. As a consequence, the electronic structure of the two models is really close to that of the bulk phase and all the manganese atoms present a magnetic moment of 3.2 μ_B as expected for Mn^{4+} within the bulk. The density of states (DOS) of

the two surface models are provided and compared to the bulk DOS in supporting information, Figure S7.

3.2.Surface reactivity with SO_2 gas probe

3.2.1. Surface characterization of the crystals after adsorption

The surface reactivity of Li_2MnO_3 was investigated through the adsorption of an SO_2 gas probe and the materials obtained after the adsorption are characterized by XPS and AES. Table 2 gives the atomic percentages of the elements deduced from the XPS analysis. The surface stoichiometry ($Li_{1.36}MnO_{1.97}$) is close to that observed before adsorption. The actual SO_2 adsorption is confirmed through the detection of Sulfur and the S 2p spectrum is shown in Figure 5. It consists of a $2p_{3/2}$-$2p_{1/2}$ doublet due to the spin-orbit coupling. We observed a unique doublet with an S $2p_{3/2}$ binding energy of 169.2 eV assigned to SO_4^{2-} species as reported by Andreu *et al.*[12] The S/Mn ratio extracted from the chemical analyses is equal to 0.1.

As a result of the SO_2 adsorption, the O 1s core peak (Figure 5) presents a significant increase of the component located at 531.9 eV due to the oxygen atom from the adsorbed SO_2 gas probe (as shown in Supporting Information, Figure S6). No obvious modification of the Li 1s core peak (Figure S6) has been observed after adsorption. However, we can notice on Figure 2 the appearance of a shoulder at 641.4 eV on the Mn $2p_{3/2}$ peak, which is characteristic of the Mn^{3+} cation. As highlighted in Supporting Information, Figure S6, the Mn 3p envelope is also modified after adsorption with the presence of Mn^{3+}. On the Mn 3s peaks, we observed a slight shift of the splitting energy value, from 4.5 to 4.8 eV, after the adsorption (Figure S5). Even if this shift evolves in the way of an increase of the Mn^{3+} oxidation state content, it is not as significant as the evolution of the Mn 2p core peaks. But, on the basis of the fact that the Mn 2p

spectra are more representative of the surface than the Mn 3s spectra, we could suggest that the Mn^{4+} cations are mainly reducible at the extreme surface after the SO_2 adsorption. Using Li_2MnO_3 and Mn_2O_3 as references for Mn^{4+} and Mn^{3+} species respectively, it was possible as described in details in Figure S4 to quantify the Mn^{3+} content, i.e. 4% ± 2% before adsorption and 19 % ± 3% after adsorption.

	B.E. (eV)	%
Mn $2p_{3/2}$	642.3	14.0
O 1s	529.8	27.6
	531.9	13.2
		40.7
C 1s	285.0	18.3
	285.6	2.6
	286,7	1.3
	288.7	1.5
		23.6
S 2p	169.2	1.7
Li 1s	54.5	20.0

Table 2. Binding energy (B.E.) of the core peaks and atomic percentages of the elements determined from XPS analyses after SO_2 adsorption.

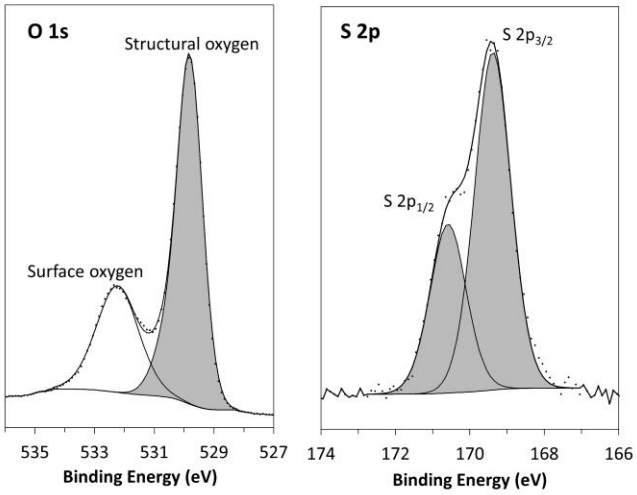

Figure 5. O 1s (left) and S 2p (right) core peaks after SO_2 adsorption reaction on the Li_2MnO_3 crystal.

The XPS analyses have shown that only sulfate species are observed on the (001) crystal surface, which suggests a redox adsorption process between the SO_2 gas probe and the material surface. This adsorption mechanism implies for charge compensation the reduction of the manganese cations sitting at the upper surface which was evidence on the Mn 2p spectra after SO_2 adsorption. As these analyses, performed twice on three adsorbed samples, have been shown reproducible, we conclude that adsorption is homogenous on the whole crystal surface. Nevertheless, as the XPS spot size is of 400×700 μm^2, Auger electron spectroscopy analyses were also performed on the same samples in order to probe the sulfur adsorption and its distribution at nanoscale (5×5 nm lateral resolution) (Figure 6).

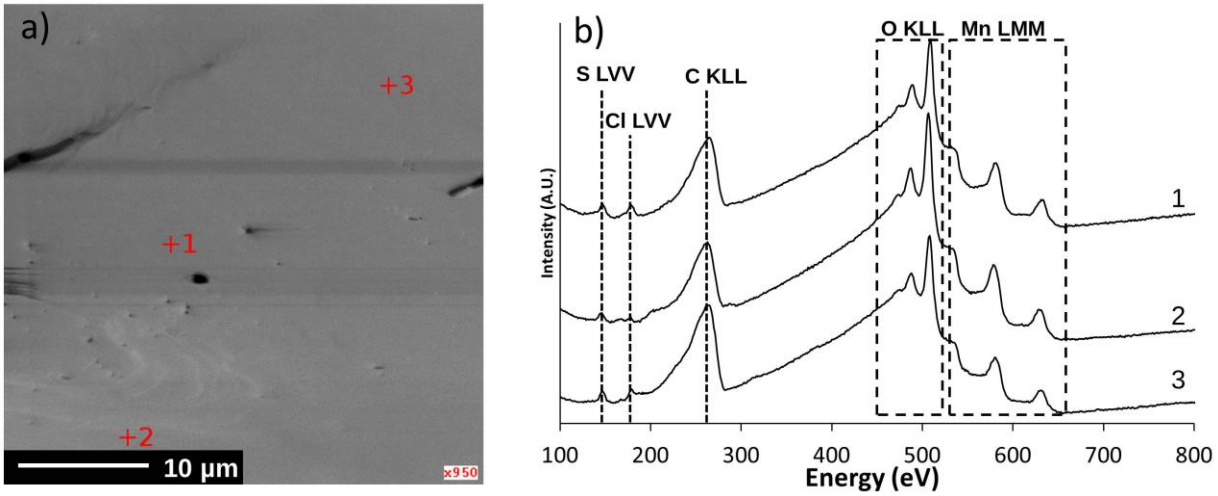

Figure 6. AES analyses of a Li_2MnO_3 crystal after SO_2 adsorption: (a) SEM image of the Li_2MnO_3 crystal surface with the analysed zones indicated by red crosses, (b) the corresponding Auger spectra.

The adsorption of sulfur is confirmed in the three zones with the detection of the S LVV transition at 140-150 eV[35], C KLL, O KLL and Mn MNN transitions are also detected at 220-280 eV, 460-520 eV and 525-645 eV respectively[35]. Chlorine was also detected at 173-183 eV which probably comes from residues of the LiCl precursor. In addition, AES chemical mapping was

carried out (Figure 7) in order to characterize the spatial elemental distribution of Mn, S and O on the whole crystal surface. The comparison of the individual chemical maps associated to Mn and S clearly confirms the homogeneity of the distribution of all the elements.

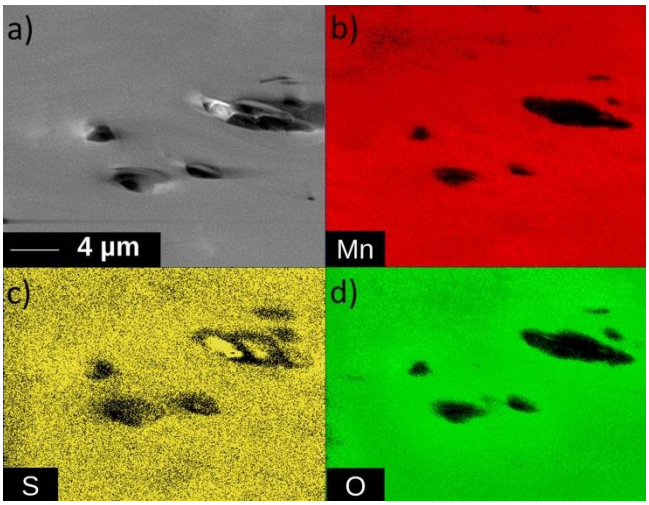

Figure 7. Auger chemical mapping of a Li_2MnO_3 crystal surface after SO_2 adsorption: (a) SEM image of the analysed area with the corresponding (b) Mn, (c) S and (d) O maps.

3.2.2. Calculations of the electronic structures

Calculations of the adsorption of an SO_2 probe molecule were performed on the two surface models described below. Sulfite and sulfate sites were probed in an exhaustive way by considering all nonequivalent oxygen atoms at the last atomic layer of the surface. In the starting structures, the SO_2 molecule is placed to obtain either a tetrahedral or a trigonal environment for the sulfur atom in the case of sulfate or sulfite sites, respectively. The initial S-O_{struct} bond lengths, where O_{struct} is an oxygen atoms belonging to the slab, were set to 1.55 Å. We present hereafter the results obtained for the most stable sulfite and sulfate adsorptions for each surface model (see Table 3). The structures obtained after relaxation of the systems are depicted in Figure 8. The adsorption energies have been calculated from equation (2) and the electronic transfers, Δq_{SO_2}, from the SO_2 molecule toward the surface, were deduced from a Bader charges

analysis. The local geometry of the adsorbed species is characterized using the Gillespie notation where AX_4, AX_3E_1 and AX_3 stand for tetrahedral, pyramidal and trigonal planar geometries respectively.

Whatever the surface model, the most stable mode of adsorption corresponds to the formation of the sulfate, as revealed by the lower adsorption energy. It is associated with a charge transfer of 0.95 to 1.22e corresponding to a redox reaction. The $S\text{-}O_{struct}$ bond lengths are in the range of 1.51 to 1.58 Å for the sulfate species, which are common values for S-O bonds, whereas the S-O bond lengths are 1.51 Å for isolated SO_4^{2-} or SO_3^{2-} at the same calculation level. The range of the adsorption energies associated to the bond length indicates that the SO_2 molecule is chemisorbed on the surface. The electronic transfer associated to the formation of sulfate species leads to the reduction of either the first atomic layer or the subsurface layer. In the case of the (001)-O surface, the excess of electron coming from the SO_2 molecule is delocalized on the whole first oxygen layer at the top of the surface. In the case of the (001)-Li surface, the electronic transfer involves several manganese atoms of the subsurface layer. The magnetic moments of these manganese atoms increase from 3.2 to 3.7 μ_B corresponding to a reduction from Mn^{4+} to an intermediate $Mn^{3+/4+}$ species.

These results agree with the interpretation of, both, the shift of the Mn 3s XPS core peaks and the shoulder at low B.E. on the Mn 2p spectrum corresponding to a reduction of the manganese atoms of the surface after the adsorption of the SO_2 molecule.

Although less energetically favorable, it is also interesting to consider the mechanisms associated to adsorption as sulfite species:

In the case of the (001)-Li surface, these species are stabilized by secondary interactions with Li atoms on the surface layer (dashed lines in Figures 8d) and exhibit a weak electronic transfer

from the surface toward the SO_2 molecule, associated to an acid-base process. After adsorption, the electronic structure of atoms belonging to the surface is unchanged.

In the case of the (001)-O surface, we identify a new adsorption process based on our previous works. As there is no cation on the last atomic layer to stabilize a sulfite specie with secondary interactions, the adsorbed species relaxes toward a trigonal planar AX_3 geometry in order to minimize the O-O repulsions. The adsorption leads to a large charge transfer of 1.27e- which indicates a redox electronic process and which is delocalized on the whole first oxygen atoms layer at the top of the surface. In the case of sulfite species, $S\text{-}O_{struct}$ bond lengths are in the range of 1.67 to 1.72 Å while intramolecular bond lengths are still between 1.51 and 1.57 Å. Because of the polarity of this surface, the adsorption energies might be overestimated, but the main result here is that without Li cations on the last surface layer, sulfate species are still the most thermodynamically favored species which reinforce the results obtained on the (001)-Li surface and the agreement with the experimental measures.

	Site	E_{ads} (eV)	Δq_{SO_2}	Geometry
(001)-O	Sulfate	-4.04	1.22	AX_4
	Sulfite	-1.75	1.27	AX_3
(001)-Li	Sulfate	-2.1	0.95	AX_4
	Sulfite	-1.7	-0.42	AX_3E_1

Table 3. Adsorption energies $\boldsymbol{E_{ads}}$ in eV, charge transfer $\boldsymbol{\Delta q_{SO_2}}$ from the SO_2 molecule towards the surface, for the two surface models and for the most stable adsorption sites. The geometry column refers to the local arrangement of oxygen atoms around the sulfur atom according to Gillespie notation.

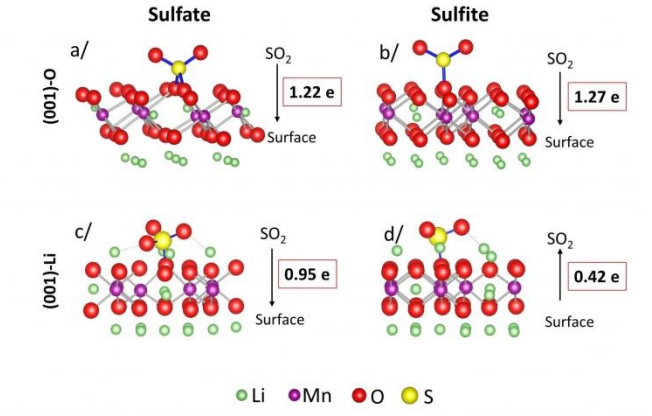

Figure 8. Structure obtained after the relaxation of the atomic position for the most stable SO_2 adsorption on the two surface models and the corresponding charge transfer from the SO_2 molecule towards the surface. Sulfite and sulfate adsorptions are depicted on the right and on the left sides of the Figure, respectively. (a) and (b) sulfate and sulfite adsorption on the (001)-O surface, respectively. (c) and (d) sulfate and sulfite adsorption on the (001)-Li surface, respectively.

4. Conclusion

The surface reactivity of a (001) oriented Li_2MnO_3 crystal was investigated through the adsorption of SO_2 gas probes, at the nanoscale from AES and first principle calculations, and at the micro-scale from SEM and XPS characterization techniques. Li_2MnO_3 crystals were synthetized by a solid path synthesis followed by a slow cooling of the samples in order to obtain large enough crystals to be able to focus the XPS beam on the top (001) surface of one of them. A chemical mapping of the surface after adsorption showed a uniform distribution of the adsorbed species. Moreover, XPS and first principle calculations evidence the energetically favorable formation of sulfate species associated to a redox process involving the reduction of manganese atoms of first surface layers of the material. The reduction of these atoms was confirmed both by the shift of the splitting value of the Mn 3s XPS core peak and by the increase of the magnetic moments of manganese atoms computed by first principle calculations. This surface reactivity can be associated to the presence of Mn^{4+} species in this material. Our strategy which combines experimental and theoretical investigation has thus proven to be relevant. Future work will focus on other valence state of manganese atoms (Mn^{3+} or mixed valence states) in order to obtain a wider overview of the relationship between the surface reactivity and the valence state of transition metals at the surface of the material.

ASSOCIATED CONTENT

Supporting Information.

The Supporting information contains Figures, Tables and description to complete and precise some points in the main manuscript. This material is available free of charge via the Internet at http://pubs.acs.org.

AUTHOR INFORMATION

Corresponding Author

*Delphine Flahaut

delphine.flahaut@univ-pau.fr

ACKNOWLEDGMENT

The authors thank the Conseil Général des Pyrénées Atlantiques and the French Research Network on the Electrochemical Energy Storage (RS2E) for funding the AQT's PhD fellowship, and Philippe Dagault (ICMCB-Pessac) for his technical support. This project received also funding from Région Nouvelle Aquitaine and the French National Research Agency (STORE-EX Labex Project ANR-10-LABX-76-01). The theoretical calculations were performed using HPC resources from GENCI-CINES (Grant 2016 – c2016086920) and the Mesocentre de Calcul Intensif Aquitain (MCIA). The acquisition of the RS2E single crystal diffractometer was also partially supported by the FEDER (European Fund for Regional Development) fund and the Picardie region.

REFERENCES

[1] Ozawa, K. Lithium-ion Rechargeable Batteries with $LiCoO_2$ and Carbon Electrodes: the $LiCoO_2$/C system. *Solid State Ionics* **1994,** 69, 212–221.

[2] Zheng, H.; Sun, Q.; Liu, G.; Song, X; Battaglia, V. S. Correlation between Dissolution Behavior and Electrochemical Cycling Performance for $LiNi_{1/3}Co_{1/3}Mn_{1/3}O_2$-based Cells. *J. Power Sources* **2012,** 207, 134–140.

[3] Lu, Z.; Dahn, J. R. Understanding the Anomalous Capacity of Li Li $[Ni_xLi(1/3-2x/3)Mn(2/3-x/3)]O2$ Cells Using In Situ X-Ray Diffraction and Electrochemical Studies. *J. Electrochem. Soc.* **2002,** 149, A815–A822.

[4] Koga, H.; Croguennec L.; Ménétrier M.; Mannessiez P.; Weill F.; Delmas C. Different Oxygen Redox Participation for Bulk and Surface: A Possible Global Explanation for the Cycling Mechanism of $Li_{1.20}Mn_{0.54}Co_{0.13}Ni_{0.13}O_2$. *J. Power Sources* **2013,** 236, 250–258.

[5] Sathiya, M.; Rousse G.; Ramesha K.; Laisa C.P.; Vezin H.; Sougrati M. T.; Doublet M. L.; Foix D.; Gonbeau D.; Walker W.; Prakash A S.; Ben Hassine M.; Dupont L.; Tarascon J.-M. Reversible Anionic Redox Chemistry in High-capacity Layered-oxide Electrodes. *Nat Mater* **2013,** 12, 827–835.

[6] Oh, Y.; Ahn, D.; Nam, S.; Park, B. The Effect of Al_2O_3-coating Coverage on the Electrochemical Properties in $LiCoO_2$ Thin Films. *J. Solid State Electrochem.* **2009**, 14, 1235–1240.

[7] Oh, S.; Lee, J. K.; Byun, D. Cho, W. I.; Won Cho, B. Effect of Al_2O_3 Coating on Electrochemical Performance of $LiCoO_2$ as Cathode Materials for Secondary Lithium Batteries. *J. Power Sources* **2004,** 132, 249–255.

[8] Huang, Y.; Chen, J.; Cheng, F.; Wan, W.; Liu, W.; Zhou, H.; Zhang, X. A Modified Al_2O_3 Coating Process to Enhance the Electrochemical Performance of $Li(Ni_{1/3}Co_{1/3}Mn_{1/3})O_2$ and its Comparison with Traditional Al_2O_3 Coating Process. *J. Power Sources* **2010,** 195, 8267−8274.

[9] Machida, N.; Kashiwagi, J.; Naito, M.; Shigematsu, T. Electrochemical Properties of All-solid-state Batteries with ZrO_2-coated $LiNi_{1/3}Mn_{1/3}Co_{1/3}O_2$ as Cathode Materials. *Solid State Ionics* **2012,** 225, 354–358.

[10] Verdier, S.; El Ouatani L.; Dedryvère R.; Bonhomme F.; Biensan P.; Gonbeau D. XPS Study on Al_2O_3- and $AlPO_4$-Coated $LiCoO_2$ Cathode Material for High-Capacity Li Ion Batteries. *J. Electrochem. Soc.* **2007,** 154, A1088–A1099.

[11] Dahéron, L.; Martinez, H.; Dedryvère, R.; Baraille, I.; Ménétrier, M.; Denage, C.; Delmas, C.; Gonbeau, D. Surface Properties of $LiCoO_2$ Investigated by XPS Analyses and Theoretical Calculations. J. Phys. Chem. C **2009,** 113, 5843−5852.

[12] Andreu, N.; Flahaut D.; Dedryvère R.; Minvielle M.; Martinez H.; Gonbeau D. XPS Investigation of Surface Reactivity of Electrode Materials: Effect of the Transition Metal. *ACS Appl. Mater. Interfaces* **2015,** 7, 6629–6636.

[13] Andreu, N.; Baraille I., Martinez H., Dedryvère R., Loudet M., Gonbeau D., New Investigations on the Surface Reactivity of Layered Lithium Oxides. *J. Phys. Chem. C* **2012,** 116, 20332–20341.

[14] Tang, W.; Kanoh, H.; Yang, X.; Ooi, K. Preparation of Plate-Form Manganese Oxide by Selective Lithium Extraction from Monoclinic Li_2MnO_3 under Hydrothermal Conditions. *Chem. Mater*. **2000,** 12, 3271–3279.

[15] Foix, D.; Sathiya, M.; McCalla, E.; Tarascon, J. M.; Gonbeau, D. X-ray Photoemission Spectroscopy Study of Cationic and Anionic Redox Processes in High-Capacity Li-Ion Battery Layered-Oxide Electrodes. *J. Phys. Chem. C* **2016,** 120, 862–874.

[16] Vallverdu, G.; Minvielle, M.; Andreu, N.; Gonbeau, D.; Baraille, I. First Principle Study of the Surface Reactivity of Layered Lithium Oxides $LiMO_2$ (M = Ni, Mn, Co). *Surf. Sci.* **2016,** 649**,** 46–55.

[17] Scofield, J. H. Hartree-Slater Subshell Photoionization Cross-sections at 1254 and 1487 eV. *J. Electron Spectrosc. Relat. Phenom.* **1976,** 8, 129–137.

[18] Kresse, G.; Furthmüller, J. Efficient Iterative Schemes for Ab initio Total-energy Calculations using a Plane-wave Basis Set. *Phys. Rev. B* **1996,** 54, 11169–11186.

[19] Kresse, G.; Hafner, J. Ab Initio Molecular-dynamics Simulation of the Liquid-Metal–Amorphous-semiconductor Transition in Germanium. *Phys. Rev. B* **1994,** 49, 14251–14269.

[20] Perdew, J. P.; Chevary J. A.; Vosko S. H.; Jackson K. A.; Pederson M. R.; Singh D. J.; Fiolhais C. Atoms, Molecules, Solids, and Surfaces: Applications of the Generalized Gradient Approximation for Exchange and Correlation. *Phys. Rev. B* **1992,** 46, 6671–6687.

[21] Perdew, J. P.; Wang, Y. Accurate and Simple Analytic Representation of the Electron-gas Correlation Energy. *Phys. Rev. B* **1992,** 45, 13244–13249.

[22] Kresse, G.; Joubert, D. From Ultrasoft Pseudopotentials to the Projector Augmented-wave Method. *Phys. Rev. B* **1999,** 59, 1758–1775.

[23] Bader, R. F. W. Atoms in Molecules. *Acc. Chem. Res.* **1985,** 18, 9–15.

[24] Dudarev, S. L.; Botton, G. A.; Savrasov, S. Y.; Humphreys, C. J.; Sutton, A. P. Electron-energy-loss Spectra and the Structural Stability of Nickel Oxide: An LSDA+U Study. *Phys. Rev. B* **1998,** 57, 1505–1509.

[25] Zhou, F.; Cococcioni, M.; Marianetti, C.; Morgan, D.; Ceder, G. First-principles Prediction of Redox Potentials in Transition-metal Compounds with LDA+U. *Phys. Rev. B* **2004,** 70, 235121.

[26] Koyama, Y.; Arai, H.; Tanaka, I.; Uchimoto, Y.; Ogumi, Z. Defect Chemistry in Layered $LiMO_2$ (M = Co, Ni, Mn, and $Li_{1/3}Mn_{2/3}$) by First-Principles Calculations. *Chem. Mater.* **2012,** 24, 3886–3894.

[27] Koyama, Y.; Tanaka, I.; Nagao, M.; Kanno, R. First-principles Study on Lithium Removal from Li_2MnO_3. *J. Power Sources* **2009,** 189**,** 798–801.

[28] Strobel, P.; Lambert-Andron, B. Crystallographic and Magnetic Structure of Li_2MnO_3. *J. Solid State Chem.* **1988,** 75, 90–98 (1988).

[29] Boulineau, A.; Croguennec, L.; Delmas, C.; Weill, F. Structure of Li_2MnO_3 with Different Degrees of Defects. *Solid State Ionics* **2010,** 180, 1652–1659.

[30] Boulineau, A.; Croguennec, L.; Delmas, C.; Weill, F. Reinvestigation of Li_2MnO_3 Structure: Electron Diffraction and High Resolution TEM. *Chem. Mater.* **2009,** 21**,** 4216–4222.

[31] Biesinger M. C.; Payne B. P.; Grosvenor A. P.; Lau L. W. M.; Gerson A. R.; St. C. Smart R. Resolving Surface Chemical States in XPS Analysis of First Row Transition Metals, Oxides and Hydroxides: Cr, Mn, Fe, Co and Ni *Appl. Surf. Sci.* **2011,** 257, 2717-2730

[32] Brabers, V. A. M.; van Setten, F. M.; Knapen, P. S. A. X-ray Photoelectron Spectroscopy Study of the Cation Valencies in Nickel Manganite. *J. Solid State Chem.* **1983,** 49, 93–98.

[33] Allen, G. C.; Harris, S. J.; Jutson, J. A.; Dyke, J. M. A study of a Number of Mixed Transition Metal Oxide Spinels using X-ray Photoelectron Spectroscopy. *Appl. Surf. Sci.* **1989,** 37, 111–134.

[34] Shin, Y.; Persson, K. A. Surface Morphology and Surface Stability against Oxygen Loss of the Lithium-Excess Li_2MnO_3 Cathode Material as a Function of Lithium Concentration. *ACS Appl. Mater. Interfaces* **2016,** 8, 25595–25602.

[35] Palmberg, P. W. Handbook of Auger Electron Spectroscopy: A Reference Book of Standard Data for Identification and Interpretation of Auger Electron Spectroscopy Data. (1972).

TOC

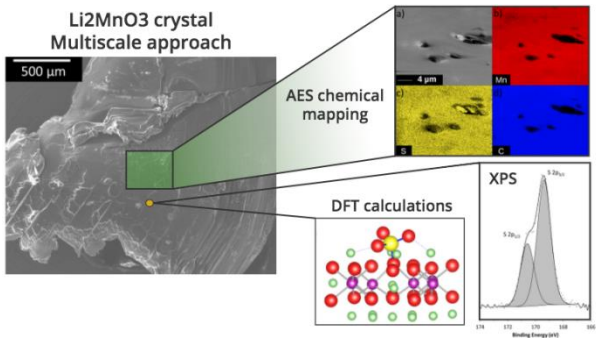
Li2MnO3 crystal
Multiscale approach
500 µm
AES chemical
mapping
4 µm
Mn
S
C
DFT calculations
XPS